Urban Flood Extent Mapping by Integrating SAR Intensity and Coherence within a Gaussian Mixture Model Framework

Rasheeda Soudagar, Alok Bhardwaj

Department of Civil Engineering, Indian Institute of Technology Roorkee, Roorkee-247667, India
Corresponding author: alok.bhardwaj@ce.iitr.ac.in (Alok Bhardwaj)

KEYWORDS: Greece floods, Interferometric coherence, Sentinel-1, Urban floods.

ABSTRACT

Urban areas are highly vulnerable to floods due to impermeable surfaces, inadequate drainage, and high population density, which intensify flood impacts. Accurate flood maps are crucial for stakeholders in disaster mitigation. In this regard, Earth observation data from active sensors like Synthetic Aperture Radar (SAR) have made significant contributions to flood delineation due to their ability to acquire data both day and night and penetrate cloud cover. However, flood mapping using only SAR backscatter in urban environments is challenging due to radar ambiguity introduced by the double bounce effect, commonly observed in inundated urban areas. Inundated regions typically appear as areas of low backscatter in SAR images, whereas flooded urban areas show a significant increase in backscatter due to the double bounce effect. This problem of under-detection caused by double bounce can be addressed by incorporating interferometric coherence (InSAR) as an additional input. Urban areas generally have high coherence, but it decreases in flooded areas. This decrease in coherence can be utilized to distinguish flooded urban areas. We present an unsupervised framework based on a Gaussian Mixture Model (GMM) that integrates intensity and coherence from Sentinel-1 SAR data to map the 2023 Greece floods. Upon validation against high-resolution optical imagery, our framework demonstrates that coherence significantly enhances urban flood mapping.

1. INTRODUCTION

Urban flooding is a growing concern worldwide, causing extensive damage to infrastructure, disrupting transportation networks, contaminating water sources, and affecting essential services in cities (Agonafir et al., 2023). This damage can be partially mitigated by implementing effective flood management strategies. Accurate and reliable flood extent maps are essential for these tasks, aiding evacuation planning and disaster response (Mishra et al., 2024). Earth observation data, such as optical and radar imagery, has been widely used for flood mapping (Shastry et al., 2023). In particular, Synthetic Aperture Radar (SAR) has proven to be an invaluable tool for flood monitoring due to its cloud-penetrating capabilities and ability to operate day and night, allowing for timely and accurate assessments of flood extents (Jiang et al., 2021). With the advancement of SAR sensors and the launch of missions offering enhanced spatial and temporal resolution, numerous flood mapping techniques have been developed.

Most of these techniques identify flooded areas by detecting regions of low backscatter, as water surfaces act as specular reflectors, deflecting the majority of radar waves away from the sensor and thereby appearing as areas of reduced backscatter in SAR image (Bhatt et al., 2020). Techniques such as histogram thresholding, clustering, and Active Contour Models (ACM) use this principle to detect floods using single SAR imagery (Soudagar et al., 2024). Another approach to quantify flood extent involves change detection, which relies on the premise that floods induce measurable changes on land surface. Change detection requires a flooded SAR image and a non-flood reference SAR image to highlight the change in pixel values caused by flood (Clement et al., 2018). This approach is useful in reducing overestimation of flood extent by effectively excluding permanent water bodies and water-like surfaces such as tarmac and shadows (Ta et al., 2024).The techniques which rely solely on SAR intensity underperform in urban environments as the radar signatures of inundated areas are ambiguous (Pulvirenti et al., 2017). In addition to specular reflections, inundated urban areas exhibit a double bounce effect, where incident radar waves reflect off the water surface, then towards vertical walls of buildings, and subsequently return as a strong backscatter signal to the sensor (Mason et al., 2010). This causes inundated urban areas to appear as regions of increased backscatter, leading to the underestimation of flood extents. The increase in backscatter values relative to non-flooded conditions can be used to detect the double bounce effect, but this detection is influenced by the orientation of buildings relative to the satellite's flight path (Delgado Blasco et al., 2020). Multiple reflections from nearby structures and strong scattering from metal surfaces produce similar backscatter enhancements that further complicate the detection.

Aforementioned shortcomings of intensity data to detect urban floods could be mitigated by integrating interferometric synthetic aperture radar (InSAR) coherence with intensity data. InSAR coherence provides the measure of correlation between two Single Look Complex (SLC) images taken from the same orbit at different times but with identical acquisition geometry (Thakur et al., 2025). Urban areas are stable targets and exhibit high coherence, but coherence reduces drastically when changes occur, such as those introduced by floods (Pierdicca et al., 2018). This relative reduction in coherence along with increase in backscatter can be effectively used to map urban floods. Reduction in coherence can be calculated through thresholding of coherence difference image. This reduction in coherence is complimented with double bounce extraction to detect urban floods (Ohki et al., 2019). Various studies have attempted to fuse SAR intensity and coherence using region growing algorithm (Pelich et al., 2022), Bayesian networks (Li et al., 2019), and machine learning models (Baghermanesh et al., 2022), though majority of these methods are supervised. VV polarization is found to perform better than VH polarization in detecting urban floods through index based approaches (Zhang et al., 2021).

This study attempts to develop an unsupervised urban flood mapping frame work by using Sentinel-1 SAR data in a Gaussian

This contribution has been peer-reviewed. The double-blind peer-review was conducted on the basis of the full paper.
https://doi.org/10.5194/isprs-annals-X-G-2025-847-2025 | © Author(s) 2025. CC BY 4.0 License.

mixture model (GMM). The framework was used to map the devastating urban floods in Larissa, Greece, during September 2023. Several studies have mapped the Greece floods of 2023 using SAR data (Theocharidis et al., 2023; Kalafatis et al., 2024; Tupas et al., 2024); however, most have focused solely on intensity-based approaches, overlooking urban flooding. Our study addresses this gap by utilizing coherence and intensity information from Sentinel-1 SAR data to map inundated urban areas. This comprehensive approach provides accurate flood maps, particularly in urban environments where conventional intensity-based methods struggle.

2. MATERIALS AND METHODS

2.1 Study Area

In the present study, we selected the September 2023 flood event that occurred in central Greece, triggered by Storm Daniel. The storm brought intense rainfall after weeks of drought, wildfires, and extreme heat in the region. Certain cities received up to 500 mm of rainfall in a single day, surpassing all previous observational records. This event is considered the most severe rainfall in Greece's recorded history and the deadliest weather-related incident of 2023, resulting in the loss of at least 17 lives. The extreme precipitation caused rivers to overflow, inundating low-lying areas in Central Greece. The study area is Larissa, one of the largest cities in Central Greece, which experienced severe inundation during this flood event (Figure 1 (a)).

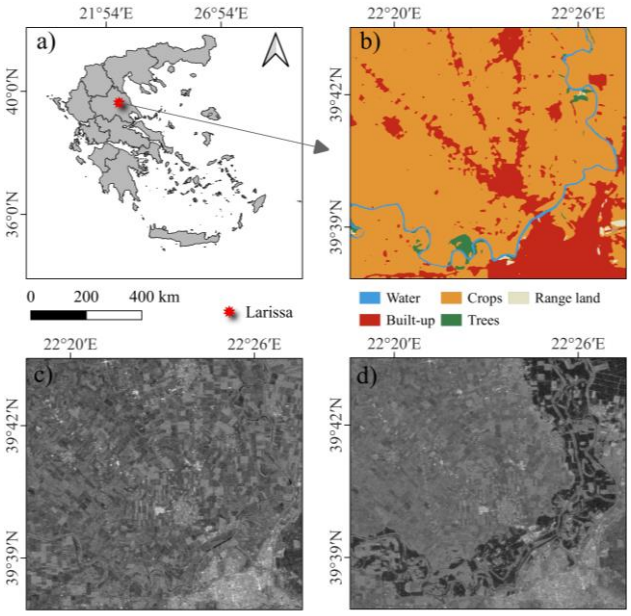

Figure 1. Study area map showing the flood effected areas of Larissa. a) Location of study area. b)10m Land Use/Land Cover (LULC) data of study area. c)Pre-flood SAR intensity image of Larissa acquired on 31/08/2023. d) During flood SAR intensity image of Larissa acquired on 12/09/2023.

2.2 Dataset

Sentinel-1 Level 1 SAR data is provided free of charge by the European Space Agency (ESA) through the Copernicus Open Access Hub (https://scihub.copernicus.eu/) and is available in two product formats: Ground Range Detected (GRD) and Single Look Complex (SLC). The GRD product contains only backscatter information, while the SLC product retains both backscatter and phase information (Soudagar et al., 2025).

Sentinel-1 products (SLC and GRD) acquired on August 19, 2023, and August 31, 2023, were used as pre-flood images, while the image acquired on September 12, 2023, was used as the during-flood image. Only VV polarization images were used in this study, as they provide better contrast between flooded and non-flooded areas, particularly in open water regions (Twele et al., 2016). Additionally, VV polarization results in a notable increase in backscatter values compared to VH polarization, particularly due to double-bounce scattering observed in inundated urban areas (Zhang et al., 2021). Land Use/Land Cover (LULC) (https://livingatlas.arcgis.com/) data extracted from Sentinel-2 data is used to extract built up area (Figure 1 (b)).

Table 1. Specifications of data used.

Data	Acquisition date	Pass Direction	Bands Used
Sentinel-1 (SLC)	19/08/2023	Ascending	VV
Sentinel-1 (SLC & GRD)	31/08/2023	Ascending	VV
Sentinel-1 (SLC & GRD)	12/09/2023	Ascending	VV
PlanetScope Optical data	12/09/2023	--	Red, Green, Blue and NIR

The final flood extents were validated against flood reference layer derived from cloud free PlanetScope optical data (https://www.planet.com/) acquired on 12 September 2023. The details of the dataset used are provided in Table 1. The SAR image acquired before and during flood are shown in Figure 1 (c) & 1 (d) respectively.

2.3 Methodology

The overview of methodology used in this work is shown in Figure 2. The work flow can be divided into three sections such as pre-processing of SAR images, application of GMM for segmenting intensity and coherence data and fusion of intensity and coherence data through logical operations to generate urban flood map.

The pre-processing steps applied on Sentinel-1 ground range detected (GRD) product to generate intensity images (31/08/2023 & 12/09/2023) include application of orbit file, thermal noise removal, calibration, speckle filtering, terrain correction and linear to decibel scale conversion.

To generate the coherence maps from SLC products the following pre-processing steps were performed: orbit file application, TOPSAR split, co-registration, coherence estimation, deburst and merge, multi-looking and terrain correction. Coherence is calculated as the normalized cross-correlation of the two co-registered SAR images (Donezar et al., 2019) (equation 1).

$$\gamma = \frac{\langle I_1 I_2^* \rangle}{\sqrt{\langle I_1 I_1^* \rangle \langle I_2 I_2^* \rangle}} \quad (1)$$

Where γ is the coherence, I_1 and I_2 represent the complex pixel values of two co-registered SLC images, * refers to the complex conjugate, and pixel values within $\langle\ \rangle$ denote spatial averaging over a given window size.

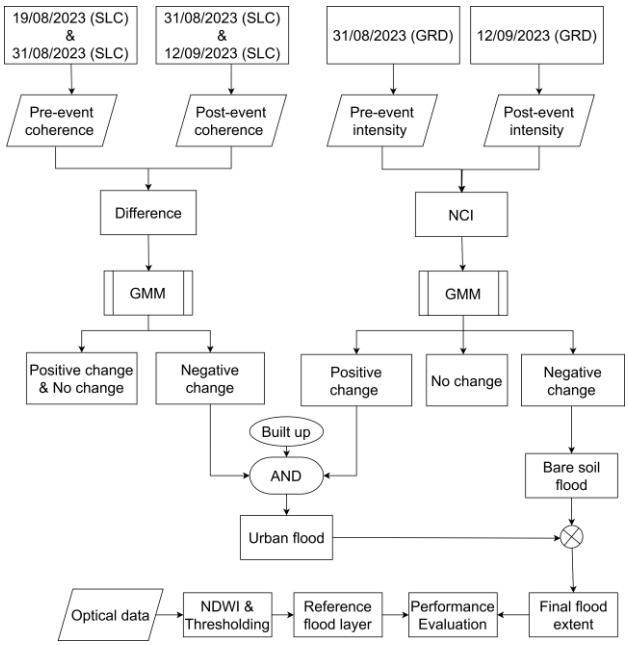

Figure 2. Methodology flow chart.

To find the coherence reduction in flooded areas, we considered: 1) two SAR images taken before the occurrence of the flood (19/08/2023 & 31/08/2023) to form pre-event coherence(γ_{pre}). 2) one image taken before flood (31/08/2023) and one during flood (12/09/2023) to form co-event coherence (γ_{co}). Using these a coherence difference image ($\gamma_{pre} - \gamma_{co}$) was formed. We hypothesize that the coherence difference image is made up of negative change class and positive & no change class. Urban areas are stable targets under no-flood conditions, resulting in high pre-event coherence values. However, the presence of floodwater causes a significant reduction in coherence due to the loss of surface stability and decorrelation, leading to low co-event coherence. This decrease in coherence makes the negative change class in the coherence difference image a reliable indicator of inundation. We segment the negative change class through GMM.

GMM is probabilistic image segmentation model, which tries to model pixel values of an image as a combination of Gaussian distributions (Celik, 2010; Guan et al., 2023). Consider an image *x* made up of *K* Gaussian distributions, then the probability density function of GMM is defined as:

$$p(x) = \sum_{k=1}^{K} \pi_k \mathcal{N}(x|\mu_k, \Sigma_k) \quad (2)$$

Where π_k is the mixing co-efficient for k^{th} Gaussian component, $\mathcal{N}(x|\mu_k, \Sigma_k)$ is Gaussian distribution with mean μ_k and covariance Σ_k. These are the parameters of GMM and are found using Expectation-Maximization (EM) algorithm.

EM algorithm involves two step estimation process:

The first step is termed as expectation step or E-step, where the algorithm calculates the responsibility γ_{ik} that component k takes for x_i.

$$\gamma_{ik} = \frac{\pi_k \mathcal{N}(x_i|\mu_k, \Sigma_k)}{\sum_{j=1}^{K} \pi_j \mathcal{N}(x_i|\mu_j, \Sigma_j)} \quad (3)$$

The second step is the maximization step or M-step, where the parameter values are updated by using responsibilities calculated in equation 3.

$$\pi_k = \frac{1}{N} \sum_{i=1}^{N} \gamma_{ik} \quad (4)$$

$$\mu_k = \frac{\sum_{i=1}^{N} \gamma_{ik} x_i}{\sum_{i=1}^{N} \gamma_{ik}} \quad (5)$$

$$\Sigma_k = \frac{\sum_{i=1}^{N} \gamma_{ik} (x_i - \mu_k)(x_i - \mu_k)^\top}{\sum_{i=1}^{N} \gamma_{ik}} \quad (6)$$

Where, *N* is the number of data points. The EM algorithm iteratively estimates the value of parameters that maximizes the likelihood function of the data ($\mathcal{L}(\theta)$).

$$\mathcal{L}(\theta) = \sum_{i=1}^{N} \log \sum_{k=1}^{K} \pi_k \mathcal{N}(x_i|\mu_k, \Sigma_k) \quad (7)$$

Besides reduction in coherence, flooded urban areas also show increased backscatter values, which can be identified by using normalized change index (NCI). NCI is a quantitative measure used to detect changes in intensity values between two SAR images acquired at different times. It helps distinguish flood-induced variations by highlighting areas with significant intensity changes (Yulianto et al., 2015; Krishna Vanama and Rao, 2019; Adhikari et al., 2023). The NCI is computed as follows (Equation 8).

$$NCI = \frac{(\sigma_1 - \sigma_2)}{(\sigma_1 + \sigma_2)} \quad (8)$$

Where σ_1 is pre-event intensity and σ_2 is during-event intensity. NCI ranges between -1 to 1. The values near to -1 indicate negative change, values close to zero represents no change and values close to 1 represent positive change. In urban areas, flooding often leads to an increase in backscatter due to the double-bounce effect, where water enhances the radar return from buildings. Thus, the positive change class corresponding to increased backscatter is segmented using GMM.

The negative change class of coherence difference image, positive change class of NCI and built-up area extracted from LULC map are merged through logical AND operation to give flooded urban areas. The final flood map is combination of urban flood map and bare soil flood map (made from negative change class of NCI).

The final flood map is validated against flood reference layer generated from optical imagery. To generate the flood reference layer, the cloud free PlanetScope image was acquired and normalized difference water (NDWI) index was formed from it using green and NIR bands (Equation 9). The NDWI image was thresholded to give the final flood reference layer.

$$NDWI = \frac{(Green - NIR)}{(Green + NIR)} \quad (9)$$

3. RESULTS AND DISCUSSIONS

The coherence difference and NCI image of Larissa which were given as input to GMM are shown in the Figure 3 (a) and (b).

The negative values of coherence difference image indicate flooded urban areas, dynamic areas and vegetated areas. Figure 4 (a) and (b) represents histogram and GMM distribution of coherence difference image. The histogram of the coherence difference image is unimodal, which complicates segmentation using traditional thresholding algorithms. In contrast, Gaussian Mixture Models (GMMs) exhibit strong unmixing potential and can effectively segment the coherence difference image into distinct classes. Hence, we applied a GMM to segment the negative change class, quantifying reduced coherence using Python programming within the Spyder IDE.

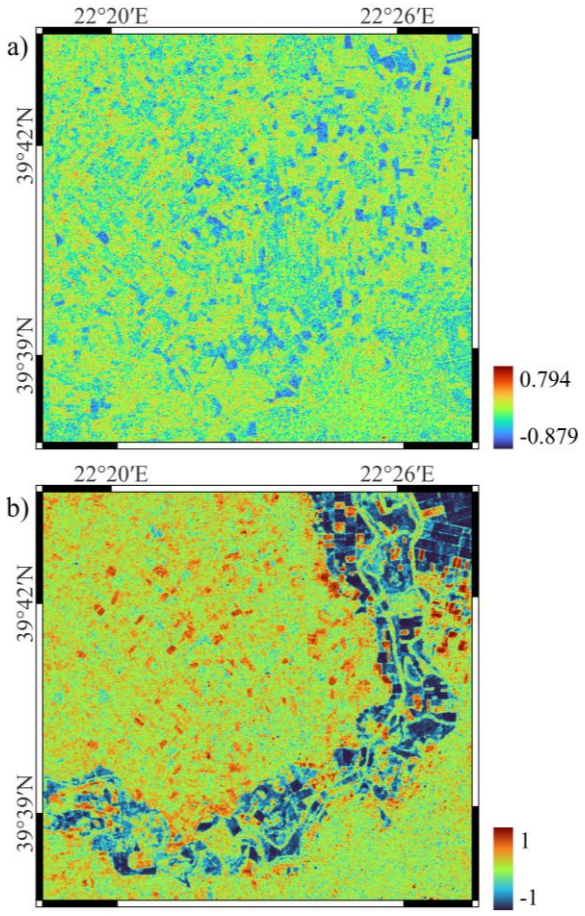

Figure 3. (a) Coherence difference image. (b) NCI image formed using intensity data.

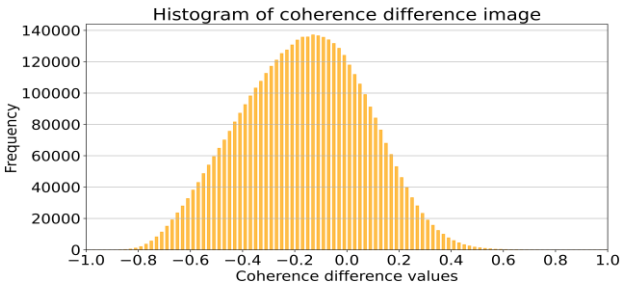

Figure 4 (a). Histogram of coherence difference image.

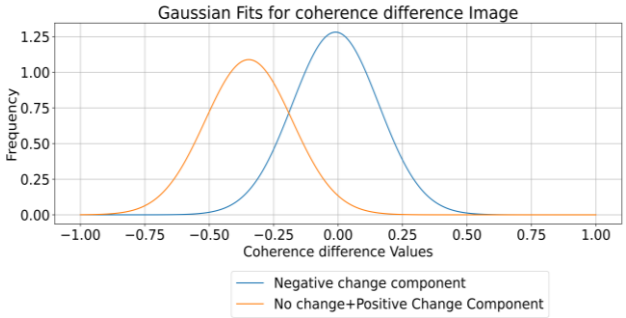

Figure 4 (b) GMM fits for coherence difference image.

The histogram and GMM modelled distributions of NCI image are shown in Fig. 5 (a) and (b). The NCI image was segmented into positive change class, negative change class, and no change class. The positive change class represents an increase in intensity values, caused by the double bounce phenomenon in inundated urban areas. The negative change class signifies a reduction in intensity values, induced by the specular reflection of floodwaters over bare soil. The no change class includes false alarms caused by targets with permanently low backscatter values, such as tarmac surfaces, shadowed areas, and permanent water bodies. These areas exhibit little to no variation in intensity values between pre and post flood conditions, leading to their classification under the unchanged class.

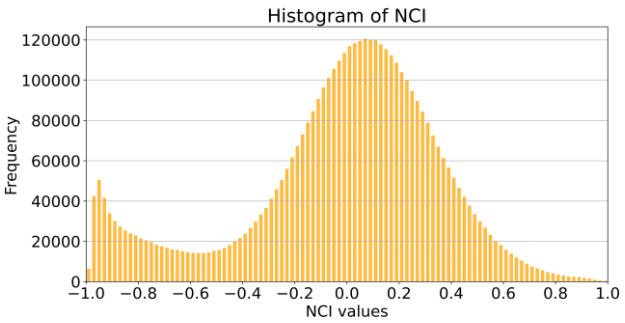

Figure 5 (a). Histogram of NCI image.

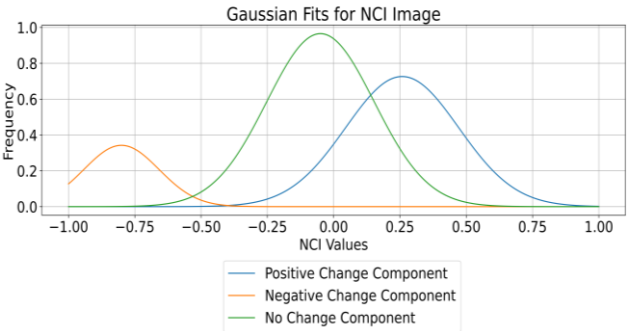

Figure 5 (b) GMM fits for NCI image.

The pixels representing negative change class of coherence difference image and pixels representing positive change class of NCI are fused by using logical operations to represent the flooded urban areas. However, this estimate includes some false positives, particularly from areas experiencing substantial non-flood-related surface changes. To eliminate these false positives built up area foot print from LULC map was used.

The final flood map generated by fusion of intensity and coherence information of SAR image is shown in figure 6 (b). The cyan pixels represent the urban flood while the red pixels denote bare soil floods. Bare soil floods are unobstructed flood surfaces which exhibit low backscatter and are delineated from NCI image by considering the negative change class.

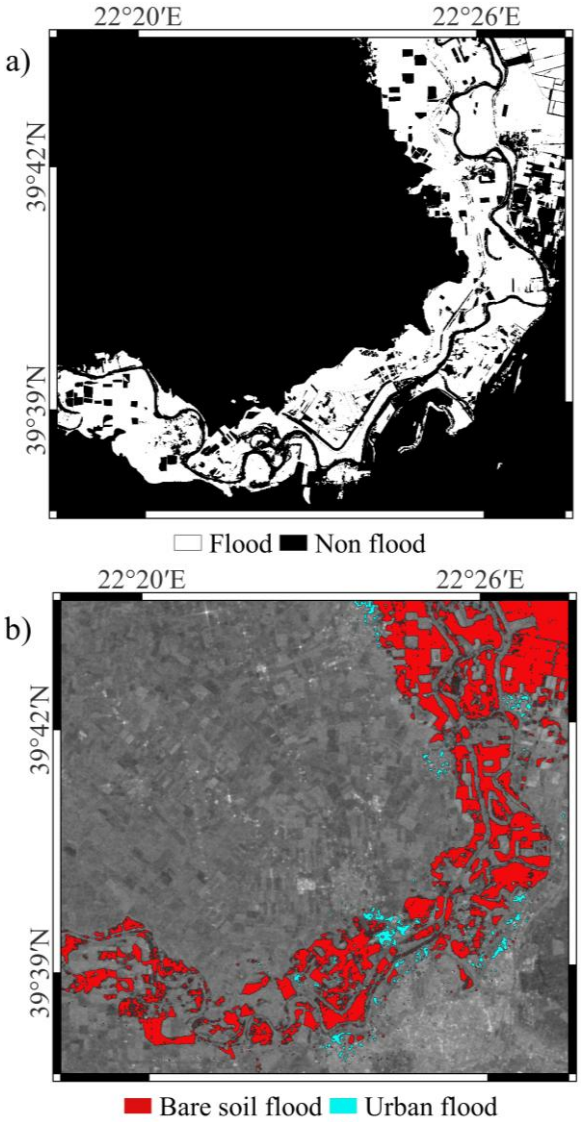

Figure 6. (a) flood reference layer. (b) final flood map.

Upon validation with flood reference layer (Fig. 6 (a)), the flood extent generated by fusing intensity and coherence information yields higher F1 score when compared to flood extents generated from intensity information only (Table 2).

Table 2. Accuracy assessment metrics for derived flood extents.

Flood map	Overall Accuracy	F1 score
Bare soil flood	86.953%	0.6521
Bare soil+Urban flood	89.849%	0.7731

4. CONCLUSIONS

In this study, we integrated intensity and coherence information from Sentinel-1 SAR data to effectively map urban floods in Larissa, Greece. Unlike state-of-the-art approaches that rely solely on intensity decrease and struggle with urban areas due to the double-bounce effect, our method leverages coherence reduction and intensity increase as key urban flood indicators, enhancing detection accuracy. Our work highlights the potential of GMM, an unsupervised probabilistic segmentation model, in integrating coherence and intensity data for robust urban flood mapping. A built-up mask was also applied to reduce false positives arising from coherence changes in vegetated and other dynamic areas. The resulting flood maps achieved an overall accuracy of 89.849% and an F1 score of 0.7731, outperforming flood maps generated solely from intensity data. The framework minimizes overestimation by excluding permanent water bodies and effectively reduces misclassifications of water-like surfaces, such as tarmac and shadows, by utilizing a change detection approach. The generated flood extents support the development of flood-resilient cities by contributing valuable insights for effective flood management efforts. This work can be further improved by integrating coherence information from both cross-polarization and co-polarization channels, thereby quantifying both double-bounce and multiple-bounce interactions in inundated urban areas, leading to more accurate flood assessments. Additionally, future research can expand this study to different geographical regions to assess the robustness and effectiveness of the proposed approach in diverse flood scenarios.

Acknowledgements

This study was supported by the project SER-1772-CED (File No. SRG/2021/001706), sponsored by SERB, New Delhi and registered at SRIC (Sponsored Research and Industrial Consultancy), Indian Institute of Technology Roorkee. The authors would like to thank ESA for providing the Sentinel-1 SAR image; PLANET for providing validation data; and ESRI for providing the land cover data.

References

Adhikari, R., Tsutsumida, N., Bhardwaj, A., 2023. An Index-Based Flood Mapping Using Stokes Parameters of Multitemporal SAR Images: 2019 Hagibis Flood Event of Ibaraki, Japan, in: IGARSS 2023 - 2023 IEEE International Geoscience and Remote Sensing Symposium. Presented at the IGARSS 2023 - 2023 IEEE International Geoscience and Remote Sensing Symposium, pp. 7194–7197. https://doi.org/10.1109/IGARSS52108.2023.10281581

Agonafir, C., Lakhankar, T., Khanbilvardi, R., Krakauer, N., Radell, D., Devineni, N., 2023. A review of recent advances in urban flood research. Water Secur. 19, 100141. https://doi.org/10.1016/j.wasec.2023.100141

Baghermanesh, S.S., Jabari, S., McGrath, H., 2022. Urban Flood Detection Using TerraSAR-X and SAR Simulated Reflectivity Maps. Remote Sens. 14, 6154. https://doi.org/10.3390/rs14236154

Bhatt, C.M., Rao, G.S., Jangam, S., 2020. Detection of urban flood inundation using RISAT-1 SAR images: a case study of Srinagar, Jammu and Kashmir (North India) floods of September 2014. Model. Earth Syst. Environ. 6, 429–438. https://doi.org/10.1007/s40808-019-00690-z

Celik, T., 2010. Image change detection using Gaussian mixture model and genetic algorithm. J. Vis. Commun. Image Represent., Large-Scale Image and Video Search: Challenges, Technologies, and Trends 21, 965–974. https://doi.org/10.1016/j.jvcir.2010.09.005

Clement, M. a., Kilsby, C. g., Moore, P., 2018. Multi-temporal synthetic aperture radar flood mapping using change detection. J. Flood Risk Manag. 11, 152–168. https://doi.org/10.1111/jfr3.12303

Delgado Blasco, J.M., Fitrzyk, M., Patruno, J., Ruiz-Armenteros, A.M., Marconcini, M., 2020. Effects on the Double Bounce Detection in Urban Areas Based on SAR Polarimetric Characteristics. Remote Sens. 12, 1187. https://doi.org/10.3390/rs12071187

Donezar, U., De Blas, T., Larrañaga, A., Ros, F., Albizua, L., Steel, A., Broglia, M., 2019. Applicability of the MultiTemporal Coherence Approach to Sentinel-1 for the Detection and Delineation of Burnt Areas in the Context of the Copernicus Emergency Management Service. Remote Sens. 11, 2607. https://doi.org/10.3390/rs11222607

Guan, H., Huang, J., Li, L., Li, X., Miao, S., Su, W., Ma, Y., Niu, Q., Huang, H., 2023. Improved Gaussian mixture model to map the flooded crops of VV and VH polarization data. Remote Sens. Environ. 295, 113714. https://doi.org/10.1016/j.rse.2023.113714

Jiang, X., Liang, S., He, X., Ziegler, A.D., Lin, P., Pan, M., Wang, D., Zou, J., Hao, D., Mao, G., Zeng, Y., Yin, J., Feng, L., Miao, C., Wood, E.F., Zeng, Z., 2021. Rapid and large-scale mapping of flood inundation via integrating spaceborne synthetic aperture radar imagery with unsupervised deep learning. ISPRS J. Photogramm. Remote Sens. 178, 36–50. https://doi.org/10.1016/j.isprsjprs.2021.05.019

Kalafatis, A., Kyriou, A., Nikolakopoulos, K., 2024. Mapping of large-scale flooding in Thessaly region using Sentinel data, in: Earth Resources and Environmental Remote Sensing/GIS Applications XV. Presented at the Earth Resources and Environmental Remote Sensing/GIS Applications XV, SPIE, pp. 80–88. https://doi.org/10.1117/12.3031474

Krishna Vanama, V.S., Rao, Y.S., 2019. Change Detection Based Flood Mapping of 2015 Flood Event of Chennai City Using Sentinel-1 SAR Images, in: IGARSS 2019 - 2019 IEEE International Geoscience and Remote Sensing Symposium. Presented at the IGARSS 2019 - 2019 IEEE International Geoscience and Remote Sensing Symposium, pp. 9729–9732. https://doi.org/10.1109/IGARSS.2019.8899282

Li, Y., Martinis, S., Wieland, M., Schlaffer, S., Natsuaki, R., 2019. Urban Flood Mapping Using SAR Intensity and Interferometric Coherence via Bayesian Network Fusion. Remote Sens. 11, 2231. https://doi.org/10.3390/rs11192231

Mason, D.C., Speck, R., Devereux, B., Schumann, G.J.-P., Neal, J.C., Bates, P.D., 2010. Flood Detection in Urban Areas Using TerraSAR-X. IEEE Trans. Geosci. Remote Sens. 48, 882–894. https://doi.org/10.1109/TGRS.2009.2029236

Mishra, V., Tiwari, A., Mishra, P.K., 2024. Floodplain Mapping Using HECRAS Model and Geospatial techniques—A Case Study of Varanasi City, in: Sharma, V.R., Chandrakanta (Eds.), Making India Disaster Resilient: Challenges and Future Perspectives. Springer International Publishing, Cham, pp. 55–68. https://doi.org/10.1007/978-3-031-50113-5_5

Ohki, M., Tadono, T., Itoh, T., Ishii, K., Yamanokuchi, T., Watanabe, M., Shimada, M., 2019. Flood Area Detection Using PALSAR-2 Amplitude and Coherence Data: The Case of the 2015 Heavy Rainfall in Japan. IEEE J. Sel. Top. Appl. Earth Obs. Remote Sens. 12, 2288–2298. https://doi.org/10.1109/JSTARS.2019.2911596

Pelich, R., Chini, M., Hostache, R., Matgen, P., Pulvirenti, L., Pierdicca, N., 2022. Mapping Floods in Urban Areas From Dual-Polarization InSAR Coherence Data. IEEE Geosci. Remote Sens. Lett. 19, 1–5. https://doi.org/10.1109/LGRS.2021.3110132

Pierdicca, N., Pulvirenti, L., Chini, M., 2018. Flood Mapping in Vegetated and Urban Areas and Other Challenges: Models and Methods, in: Refice, A., D’Addabbo, A., Capolongo, D. (Eds.), Flood Monitoring through Remote Sensing. Springer International Publishing, Cham, pp. 135–179. https://doi.org/10.1007/978-3-319-63959-8_7

Pulvirenti, L., Chini, M., Pierdicca, N., Boni, G., 2017. Detection of flooded urban areas using sar: An approach based on the coherence of stable scatterers, in: 2017 IEEE International Geoscience and Remote Sensing Symposium (IGARSS). Presented at the 2017 IEEE International Geoscience and Remote Sensing Symposium (IGARSS), pp. 5701–5704. https://doi.org/10.1109/IGARSS.2017.8128302

Shastry, A., Carter, E., Coltin, B., Sleeter, R., McMichael, S., Eggleston, J., 2023. Mapping floods from remote sensing data and quantifying the effects of surface obstruction by clouds and vegetation. Remote Sens. Environ. 291, 113556. https://doi.org/10.1016/j.rse.2023.113556

Soudagar, R., Chowdhury, A., Bhardwaj, A., 2025. Enhanced large-scale flood mapping using data-efficient unsupervised framework based on morphological active contour model and single synthetic aperture radar image. J. Environ. Manage. 380, 124836. https://doi.org/10.1016/j.jenvman.2025.124836

Soudagar, R., Chowdhury, A., Bhardwaj, A., 2024. Application of Morphological Active Contour Model for Flood Extent Mapping Using Unitemporal SAR Image: 2023 North Indian Floods, in: IGARSS 2024 - 2024 IEEE International Geoscience and Remote Sensing Symposium. Presented at the IGARSS 2024 - 2024 IEEE International Geoscience and Remote Sensing Symposium, pp. 1200–1204. https://doi.org/10.1109/IGARSS53475.2024.10642552

Ta, L., Yu, C., Li, Z., Hu, X., Song, C., Huang, W., Zhou, M., 2024. Dynamic flood mapping by a normalized probabilistic classification method using satellite radar amplitude time series. GIScience Remote Sens. 61, 2380125. https://doi.org/10.1080/15481603.2024.2380125

Thakur, A.K., Garg, R.D., Jain, K., 2025. An assessment of different line-of-sight and ground velocity distributions for a comprehensive understanding of ground deformation patterns in East Jharia coalfield. Remote Sens. Appl. Soc. Environ. 37, 101446. https://doi.org/10.1016/j.rsase.2024.101446

Theocharidis, C., Argyriou, A.V., Tsouni, A., Kaskara, M., Kontoes, C., 2023. Comparative analysis of Sentinel-1 and PlanetScope imagery for flood mapping of Evros River, Greece, in: Ninth International Conference on Remote Sensing and Geoinformation of the Environment (RSCy2023). Presented at the Ninth International Conference on Remote Sensing and Geoinformation of the Environment (RSCy2023), SPIE, pp. 465–474. https://doi.org/10.1117/12.2682775

Tupas, M.E., Roth, F., Bauer-Marschallinger, B., Wagner, W., 2024. Assessment of time-series-derived no-flood references for sar-based Bayesian flood mapping. GIScience Remote Sens. 61, 2427304. https://doi.org/10.1080/15481603.2024.2427304

Twele, A., Cao, W., Plank, S., Martinis, S., 2016. Sentinel-1-based flood mapping: a fully automated processing chain. Int. J. Remote Sens. 37, 2990–3004. https://doi.org/10.1080/01431161.2016.1192304

Yulianto, F., Sofan, P., Zubaidah, A., Sukowati, K.A.D., Pasaribu, J.M., Khomarudin, M.R., 2015. Detecting areas affected by flood using multi-temporal ALOS PALSAR remotely sensed data in Karawang, West Java, Indonesia. Nat. Hazards 77, 959–985. https://doi.org/10.1007/s11069-015-1633-x

Zhang, H., Qi, Z., Li, X., Chen, Y., Wang, X., He, Y., 2021. An Urban Flooding Index for Unsupervised Inundated Urban Area Detection Using Sentinel-1 Polarimetric SAR Images. Remote Sens. 13, 4511. https://doi.org/10.3390/rs13224511